

Journal of Materials Chemistry C

Accepted Manuscript



This is an *Accepted Manuscript*, which has been through the Royal Society of Chemistry peer review process and has been accepted for publication.

Accepted Manuscripts are published online shortly after acceptance, before technical editing, formatting and proof reading. Using this free service, authors can make their results available to the community, in citable form, before we publish the edited article. We will replace this *Accepted Manuscript* with the edited and formatted *Advance Article* as soon as it is available.

You can find more information about *Accepted Manuscripts* in the [Information for Authors](#).

Please note that technical editing may introduce minor changes to the text and/or graphics, which may alter content. The journal's standard [Terms & Conditions](#) and the [Ethical guidelines](#) still apply. In no event shall the Royal Society of Chemistry be held responsible for any errors or omissions in this *Accepted Manuscript* or any consequences arising from the use of any information it contains.

Bi₂S₃ nanowire networks as electron acceptor layers in solution-processed hybrid solar cells

Cite this: DOI: 10.1039/x0xx00000x

Luisa Whittaker-Brooks,^a Jia Gao,^a Anna K. Hailey,^a Conor R. Thomas,^b Nan Yao,^c and Yueh-Lin Loo^{ac}

Received 00th January 2012,
Accepted 00th January 2012

DOI: 10.1039/x0xx00000x

www.rsc.org/

We report the assembly of Bi₂S₃ into percolated networks. Subsequent infiltration of poly(3-hexylthiophene), P3HT, as the electron donor generates an inorganic-organic active layer. Inverted solar cells fabricated with these active layers exhibit power-conversion efficiencies as high as 3.3%. To the best of our knowledge, this is the first example of a hybrid solar cell comprising a percolated network of single-crystalline Bi₂S₃ nanowires and P3HT.

Introduction

The photovoltaic field has witnessed dramatic changes with the development of a fourth generation of solar cells comprised of both inorganic and organic materials.¹ These so-called fourth generation solar cells have sparked research to develop hybrid organic-inorganic materials that show high photovoltaic performance at relatively low cost by leveraging the inherent attributes of both the inorganic and organic constituents. In recent years, much effort has been devoted to developing new synthetic routes for both inorganic and organic semiconductors that can effectively serve as either electron donors or acceptors in hybrid solar cells. From the organic side, for example, there has been substantial progress in the development of low-bandgap molecular and polymeric semiconductors to more effectively harness sunlight.²⁻⁵ Efforts in inorganic semiconductors have focused on the production of nanostructures since the optoelectronic properties of these nanoscale building blocks can show strong quantum-confinement effects.⁶

Several types of hybrid inorganic-organic solar cells have been fabricated employing various inorganic nanostructures, such as CdSe nanoparticles,⁷⁻⁹ CdS nanoparticles,¹⁰ TiO₂ nanorods,¹¹⁻¹³ WO₃ nanowires,¹⁴ Sb-doped SnO₂ nanowires,¹⁵ and ZnO nanowire

arrays,¹⁶⁻²² intermixed with semiconducting polymers. Efficiencies ranging from 2-5% have been obtained, positioning the performance of these hybrids close to the power conversion efficiencies (PCEs) of all organic solar cells comprising P3HT and PCBM as the donor and acceptor, respectively.^{23, 24} Although the inorganic constituents in these devices have large bandgaps and have been demonstrated to be effective electron accepting materials, they have not overcome any of the limitations encountered with fullerene derivatives, such as poor photocarrier generation due to their limited absorption in the Vis-NIR region.²⁵ To overcome this challenge, researchers have focused on the synthesis of low bandgap metal chalcogenide nanostructures to increase the spectral response of such devices. Low bandgap metal chalcogenide nanoparticles, such as PbS quantum dots,^{26, 27} PbSe quantum dots,²⁸ CuInS₂ nanoparticles,²⁹ CuO nanoparticles,³⁰ Bi₂S₃ nanocrystals,³¹⁻³⁵ and FeS₂ nanoparticles,³⁶ have been recently incorporated into hybrid-inorganic solar cells achieving efficiencies as high as 5%. Nonetheless, the hybrid solar cells comprising these nanostructures are limited by inefficient electron transport from one discrete nanostructure to another within a contiguous polymer donor matrix.^{10, 37, 38} Amongst these inorganic nanostructures, Bi₂S₃ has been recognized as a key player in the fabrication of devices for solar energy conversion,^{31-33, 39}

thermoelectric technologies,⁴⁰⁻⁴² and optoelectronics in the IR region due to its low toxicity, low bandgap (1.3–1.7 eV, which facilitates broad coverage of the solar spectrum),^{43, 44} and strong absorptivity (10^5 cm^{-1}).³²

Although Bi_2S_3 has been demonstrated to function as the active ingredient in a photodetector with a photoconductivity gain of 10^{45} , the photovoltaic characteristics of devices comprising Bi_2S_3 remain sub-optimal, with hybrid devices demonstrating PCEs $< 1\%$ ^{31, 33} when compared to devices comprising other metal chalcogenides. In recent years, several groups have tried to address - without much success - the low PCEs of hybrid solar cells comprising Bi_2S_3 as the acceptor and P3HT as the donor.³³ These low PCEs have been attributed to the polycrystalline nature of and the presence of surface defects on Bi_2S_3 nanostructures;³³ poor intermixing between the organic and the inorganic semiconducting nanostructures; and the absence of a percolated transport path for electrons between individual Bi_2S_3 nanostructures.^{31, 46} In view of these challenges, single-crystal Bi_2S_3 nanostructures in the form of nanowires have been prepared from metal salts and a sulfur source^{47, 48} or from single-source precursors⁴⁹⁻⁵¹ either by chemical-vapor deposition, sonochemical or hydrothermal procedures. Yet, we are unaware of any successful integration of such single-crystalline Bi_2S_3 nanostructures in functional devices to-date.

In this paper, we utilize a vacuum-filtration process -similar to that reported to fabricate carbon nanotubes networks⁻⁵² for the deposition of single-crystalline Bi_2S_3 nanowires into percolated networks to construct hybrid organic-inorganic solar cells. This technique offers two main advantages, i.e., it ensures an interconnected network of nanowires before the deposition of the organic component and it provides the ability to control the aggregation of inorganic nanowires. We fabricated inorganic-organic solar cells by spin-coating P3HT solutions atop the Bi_2S_3 nanowire networks. By controlling the concentrations of both the Bi_2S_3 dispersion and the P3HT solution, we can tailor the overall active layer thickness, which has allowed us to better balance electron and hole transport. This approach takes advantage of the high aspect ratio, high electron mobility, and complementary photon absorption of Bi_2S_3 nanowires and P3HT, while preserving solution processability of the active layers. We further discuss the role of morphology and optoelectronic properties of percolated Bi_2S_3 networks on the photovoltaic performance of Bi_2S_3 :P3HT hybrid solar cells.

Experimental Section

Synthesis of Bi_2S_3 nanowires

Bi_2S_3 nanowires were synthesized via a solvothermal approach. Briefly, 500 mg of bismuth nitrate pentahydrate (ACROS organics-AC40261) was dissolved in ethylene glycol. This solution was heated at 60 °C and stirred for 30 min until homogeneous and clear. Subsequently, 2 mL of 2-mercaptoethanol was added to the clear solution. The solution was then transferred to a 25 mL teflon-lined stainless-steel autoclave. The autoclave was sealed and kept at 150 °C for 24 hr. After the reaction, the resulting black product was cooled to room temperature and washed repeatedly with copious amounts of isopropanol. Finally, the product was vacuum-dried at 60 °C for 6 hr.

Fabrication of Bi_2S_3 percolated networks

We adopted a vacuum-filtration technique previously used to fabricate carbon nanotube networks to process the Bi_2S_3 nanowires.⁵² The as-synthesized Bi_2S_3 nanowires were suspended in isopropanol at a concentration of 0.1 mg mL⁻¹. 25 mL of this Bi_2S_3 solution was vacuum-filtered over a nitrocellulose membrane (Millipore, 0.22 μm GSWP). After filtration, the nitrocellulose membrane comprising Bi_2S_3 nanowires was pressed against a pre-patterned ITO on glass substrate that had been coated with TiO_x ⁵³ (with the nanowire network facing TiO_x). Subsequently, the membrane-substrate stack was exposed to an acetone-vapor bath for 1.5 hrs to dissolve the nitrocellulose, leaving behind the nanowires on TiO_x . The substrate along with the transferred Bi_2S_3 nanowires was then rinsed in liquid acetone and methanol to remove any residual nitrocellulose. We can tune the network thickness by varying the concentration of Bi_2S_3 dispersion prior to deposition. Thicknesses of 50, 140, 200, and 240 nm, for example, were obtained when 25 mL of Bi_2S_3 solutions having concentrations of 0.02, 0.05, 0.1 and 0.12 mg mL⁻¹ were vacuum-filtered over a nitrocellulose membrane. All thicknesses (including neat Bi_2S_3 nanowire networks, P3HT films, and active layers) were determined by atomic force microscopy (AFM). We further corroborated these values by measuring the average heights of our layers via cross-sectional scanning electron microscopy (SEM).

Characterization

Transmission electron microscopy studies (TEM)

A Philips CM200 FEG-TEM equipped with a Gatan 678 Imaging Filter and operated at 200 keV was used to acquire high-resolution TEM images and selected area electron diffraction (SAED) patterns. To prepare the samples for TEM/SAED analysis, the Bi₂S₃ nanowires were dispersed in 2-propanol and then deposited onto 300 mesh holey carbon-coated Cu grids.

Scanning electron microscopy studies (SEM)

An SEM equipped with a field-emission gun (FE-SEM Quanta 400 FEG, FEI) was used to image the morphology and structure of Bi₂S₃ networks. The accelerating voltage was kept at 15 keV to prevent beam damage to the specimens.

Grazing-incidence X-ray diffraction studies (GIXD)

GIXD experiments were conducted at the G1 station (10.0 ± 0.1 keV) of the Cornell High Energy Synchrotron Source. The beam was selected to be 0.05 mm tall and 1 mm wide. The width of the samples was 0.5 cm; this smaller sample width was chosen to reduce geometric smearing of crystalline reflections.⁵⁴⁻⁵⁶ The beam energy was selected with synthetic multilayer optics (W/B4C, 23.6 Å *d*-spacing). The X-ray beam was aligned above the film's critical angle but below that of the substrate equivalent to 0.32° from the substrate. The scattered intensity was collected with a two-dimensional CCD detector. All GIXD images have been background subtracted; polarization and adsorption corrections were also applied, though these corrections were small.⁵⁴⁻⁵⁶

X-ray photoelectron (XPS) and ultraviolet photoelectron (UPS) spectroscopies studies

XPS data were collected using a VG ESCALab Mk.II hemispherical analyzer and a Mg K α (1253.6 eV) source. A pass energy of 100 eV was used for survey scans, while a 20 eV pass energy was used for detailed scans. All measurements were carried out at normal take-off angles. The acquired spectra were calibrated against the adventitious carbon peak at 284.6 eV. Curve fitting was carried out using CasaXPS software with a Gaussian-Lorentzian product function and a non-linear Shirley background. The vacuum system is also equipped with He I (21.22 eV) and He II (40.81 eV)

discharge lamps for performing UPS measurements. The energy resolution of the UPS system is 150 meV, as determined from the width of the Fermi edge on a freshly deposited Au surface.

Device fabrication

Bi₂S₃ networks:P3HT solar cells

To assemble Bi₂S₃:P3HT active layers, a solution of P3HT (Merck Chemical Ltd.) in chlorobenzene at 25 mg mL⁻¹ was spin-coated at 500 rpm for 60 s atop the Bi₂S₃ percolated networks. The combined active layer of Bi₂S₃ nanowire network and P3HT was 320-nm thick. Successively, a 7-nm thick layer of MoO₃ was thermally evaporated atop the active layer. To complete the solar cells, a 100-nm thick layer of Au was deposited by thermal evaporation through stencil masks as top electrodes. The active area for each device was 0.18 cm². After device fabrication, the completed solar cells were annealed at 150°C for 10 min to induce further infiltration and crystallization of the polymer. Current density-voltage (J-V) characteristics were acquired using a Keithley 2400 source measurement unit under AM 1.5G 100 mW/cm² illumination in air.

Results and discussion

The ability to control the size, shape, and composition of Bi₂S₃ nanostructures is imperative for investigating their intrinsic optoelectronic properties. Prior to the assembly of Bi₂S₃ into percolated networks, we performed rigorous morphological and structural characterization of the as-synthesized Bi₂S₃ nanowires. From the morphological and structural characterization presented in **Figure S1** of the supporting information, we can ascertain that our nanowires are phase-pure and dimensionally-uniform having an average length of 25 ± 5 μm and an average diameter of 30 ± 5 nm. Transmission electron microscopy (TEM) measurements provided additional insight on the structure of the Bi₂S₃ nanowires. **Figure 1A** displays a representative TEM image of the nanowires dispersed on a holey carbon film supported on a Cu-TEM grid. **Figure 1B** shows a lattice-resolved high-resolution TEM image of a Bi₂S₃ single-nanowire tilted along its *c*-axis. This image shows the presence of two-dimensional lattice fringes in the Bi₂S₃ nanowire. The absence of any grain boundaries suggests that the as-synthesized nanowire is single-crystalline in nature. The crystal planes that are parallel and perpendicular to the fast growth direction of the

nanowire have observed lattice spacings of 7.96 Å and 3.98 Å, corresponding to the characteristic spacings of the (110) and (001) planes, respectively, of the orthorhombic Bi_2S_3 unit cell. Furthermore, fast Fourier transform (FFT) of an image taken along the [-110] direction reveals distinct spots, further verifying that the obtained structures are single-crystalline in nature. The FFT images also confirm our identification of the (110) and (001) planes. Collectively, the high-resolution TEM and the FFT images indicate that growth of the Bi_2S_3 nanowires take place along the [001] direction.

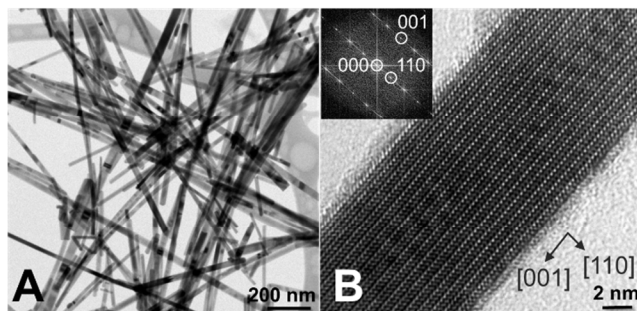


Figure 1. A) TEM image for Bi_2S_3 nanowires dispersed on a holey carbon film supported on a Cu-TEM grid. B) Lattice-resolved high-resolution TEM image of an individual Bi_2S_3 nanowire. The image shows that the [001] direction is the fast-growth direction (or the nanowire axis). The inset depicts the FFT of the nanowire lattice image viewed along the [-110] zone axis. The distinct spots observed in the inset indicate that the nanowire is single crystalline in nature.

Electrical characterization of individual Bi_2S_3 nanowires in field-effect transistors (**Figure S2**) shows that Bi_2S_3 nanowires behave as an n-type semiconductor with an estimated field-effect electron mobility of $1.3 \text{ cm}^2\text{V}^{-1}\text{s}^{-1}$. In addition, UV-Vis absorption and UPS measurements allowed us to determine the electronic properties of our Bi_2S_3 nanowire networks. From the absorption data presented in **Figure S3**, we estimated an optical bandgap of 1.2 eV for our Bi_2S_3 nanowire networks. We obtained a work function of 4.8 eV by extrapolating the cut-off energy from the UPS spectrum presented in **Figure S4A**. From the same UPS data, we can also determine a valence band edge of 5.4 eV (**Figure S4B**). This calculated valence band edge is comparable to reported values for Bi_2S_3 nanorods.³³ Based on the energy levels of Bi_2S_3 and published energy levels of P3HT,⁵⁷⁻⁶¹ a type-II heterojunction should form between P3HT and Bi_2S_3 .

Several methods of depositing Bi_2S_3 dispersions, such as drop-casting, spin-coating and dip-casting, were investigated to reliably

fabricate Bi_2S_3 networks. These methods, however, lacked control over the average network thickness, often resulting in aggregation of the nanowires and non-uniform networks. On the other hand, vacuum filtering a dilute suspension of nanowires over a porous cellulose filtration membrane resulted in uniform networks of Bi_2S_3 nanowires whose average thickness can be varied by tuning the concentration of the dispersion. **Figure 2** shows SEM micrographs of three networks (A, B, and C) that have been prepared with different concentrations of Bi_2S_3 nanowire dispersions (25, 45, and 63 wt%, respectively). As evidenced in **Figure 2**, the long axes of the nanowires in these networks appear to be randomly oriented in the plane of the substrate. The nanowires, even in the least dense (50 nm thick) Bi_2S_3 network (**Figure 2A**), remain well dispersed over large areas and percolated over macroscopic distances. **Figure 2B** shows a denser Bi_2S_3 network with an average thickness of 140 nm, whereas **Figure 2C** depicts an SEM image of a network whose average thickness is 200 nm. These images demonstrate our ability to control the spatial uniformity and network thickness via this vacuum-filtration technique.

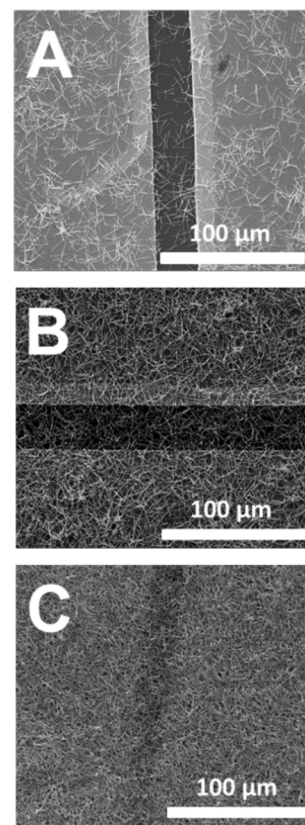


Figure 2. SEM images of vacuum-filtered Bi_2S_3 nanowire networks with average thicknesses of A) 50 nm, B) 140 nm, and C) 200 nm.

These networks form percolated pathways that allow charge conduction over macroscopic distances.

We further characterized these percolated Bi_2S_3 networks via XPS to verify that Bi_2S_3 is not chemically oxidized during the vacuum-filtration process. **Figure 3** shows the XPS spectra of a 140 nm-thick Bi_2S_3 nanowire network. The two strong peaks at ≈ 158.0 and 163.2 eV (**Figure 3A**) are assigned to $\text{Bi}_{4f_{7/2}}$ and $\text{Bi}_{4f_{5/2}}$, respectively.^{51, 62} The smaller pair of doublets at 160.5 eV and 161.7 eV correspond to the binding energies of $\text{S}_{2p_{3/2}}$ and $\text{S}_{2p_{1/2}}$, respectively.⁶² The peak at 224.8 eV, in **Figure 3B** can be assigned to S_{2s} .^{51, 62} A small peak at 227.8 eV is observed; we ascribe it to unreacted thiols from the 2-mercaptoethanol precursor used in the synthesis of our Bi_2S_3 nanowires.⁶³ Taking into account the atomic sensitivity factors of Bi and S⁶⁴ during quantification of the peak areas of Bi 4f and S 2s, the atomic ratio of Bi/S is approximately 1.4. This ratio is in close agreement with the expected ratio of 1.5 for stoichiometric Bi_2S_3 . No other peaks were observed in the full XPS spectrum indicating the absence of impurities in the percolated Bi_2S_3 network.

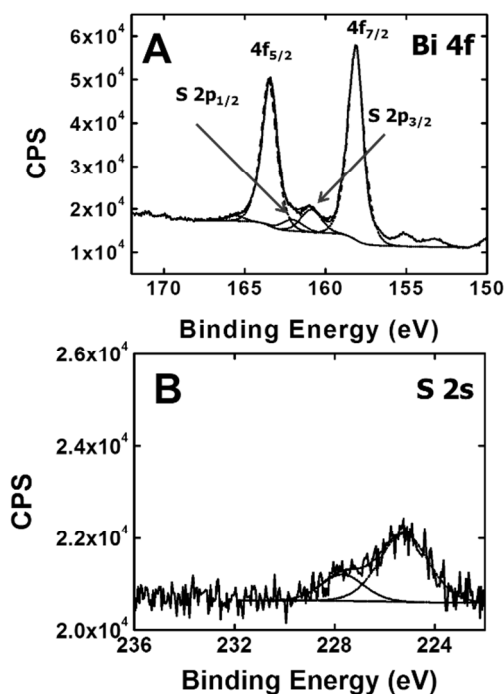


Figure 3. XPS spectra for a 140-nm thick Bi_2S_3 nanowire network. High-resolution scans of the A) Bi 4f and B) S 2s regions.

We fabricated inverted solar cells (inset in **Figure 4** shows the device architecture) by varying the thicknesses of the Bi_2S_3 and P3HT layers. We focused on creating and testing solar cells with

three different layer thicknesses of percolated Bi_2S_3 networks, i.e., 50, 140, and 200 nm as the electron acceptor layer. We also varied the P3HT layer thickness. This exercise led to devices with PCEs ranging from 0.46–3.3% (the complete device characteristics of these devices are tabulated in **Table S1**). The maximum PCE was achieved with a 200 nm-thick Bi_2S_3 network with a 120 nm-thick P3HT overlayer. The current-voltage characteristics of one such device under illumination is shown in **Figure 4A**. Of 24 devices tested across six chips, the average open-circuit voltage (V_{oc}) is 0.7 ± 0.01 V; the average short-circuit current density (J_{sc}) is 10.7 ± 0.1 mA cm⁻²; and the fill factor (FF) is 45 ± 5 %, resulting in an average PCE of 3.3 ± 0.2 %. Neglecting the presence of interfacial dipoles and vacuum level shifts^{60, 61} when Bi_2S_3 and P3HT are brought into contact, the offset between the Bi_2S_3 conduction band edge and P3HT HOMO level in **Figure S5** suggests a maximum V_{oc} of 1.0 eV. Our V_{oc} of 0.7 V is not consistent with the energy diagram, especially considering other possible origins of losses⁶⁵ and is comparable with values reported in the literature for polycrystalline Bi_2S_3 -based devices.³³ Our photocurrents, however, are substantially higher. To ensure that the photocurrents are reflective of that of individual devices, we have taken measures to eliminate a potential overestimation of the short circuit current.⁶⁶ Testing in the presence of a stencil mask ensured a well-defined illuminated area; these measurements also yielded comparable photocurrents. Among devices with optimal active layer thicknesses, we attribute the high photocurrent to the quality of Bi_2S_3 nanowires and interfacial compatibility of P3HT with Bi_2S_3 in our devices in addition to the interconnectedness of P3HT and Bi_2S_3 nanowire networks. While still not competitive amongst the highest efficiencies of hybrid inorganic-organic solar cells,^{67–71} our devices exhibit the highest efficiencies amongst those reported for hybrid solar cells comprising Bi_2S_3 nanostructures and P3HT.^{31–33, 72} Our FF, however, is consistently low, at 45%. We suspect the low but consistent FF in our devices to stem from substantial carrier recombination because of unbalanced charge transport given the mismatch in mobilities between Bi_2S_3 nanowires and P3HT.

Further verification that our photocurrents are those of individual cells stem from external quantum efficiency (EQE) measurements. We have included in **Figure 4B** the EQE spectrum for the same device whose J-V characteristics are shown in **Figure 4A**. Integration of the EQE spectrum resulted in an estimated J_{sc} of 9.5 mA cm⁻². This value is in close agreement with the measured J_{sc} extracted from the J-V characteristics. The device shows a broad

EQE spectrum spanning a wavelength range of 300–720 nm. A maximum EQE of 62% is observed in a range of 490–550 nm; photocurrent generation at these wavelengths is attributed to photoabsorption and current generation by P3HT. As evidenced in our EQE spectrum, we also observe current generation beyond the band gap of P3HT at > 650 nm. This contribution to the overall photocurrent, however, is small.

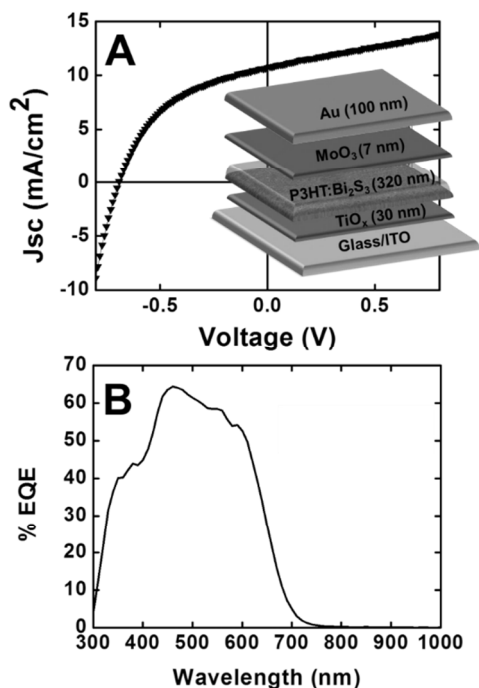


Figure 4. A) J–V characteristics under simulated AM1.5G illumination of a photovoltaic device comprised of a 200-nm thick Bi_2S_3 nanowire network and a 120-nm thick P3HT layer. The inset shows the inverted device architecture. B) EQE spectrum as a function of the wavelength of monochromatic irradiation for the device whose J–V characteristics are shown in (A).

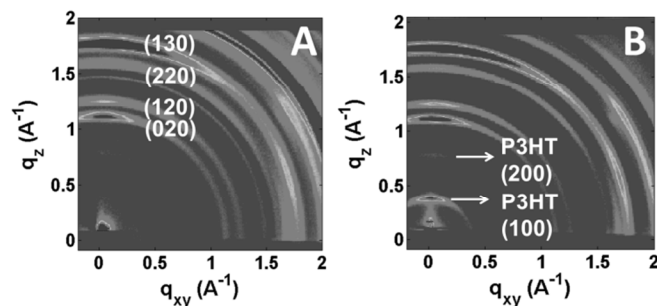


Figure 5. Two-dimensional GIXD images for A) a Bi_2S_3 nanowire network prior to P3HT deposition and B) the photoactive layer (Bi_2S_3 :P3HT) prior to top electrode deposition. For clarity, we have labelled the reflections associated with Bi_2S_3 in (A) as well as the

(100) and (200) reflections of P3HT at q (scattering vector) = 0.37 \AA^{-1} and 0.74 \AA^{-1} , respectively, in (B).

Questions, however, remain about the morphology of the Bi_2S_3 :P3HT active layer. In an attempt to elucidate the structure, we conducted additional characterization of the active layer. **Figure 5A** shows an indexed two-dimensional grazing-incidence X-ray diffraction (GIXD) image of a Bi_2S_3 network. As shown, these networks are crystalline and display out-of-plane reflections – albeit with a broad distribution of orientations ($\pm 30^\circ$) centered about the meridian – associated with the (020), (120), (220), and (130) planes of the orthorhombic unit cell belonging to the Pbnm space group of single-crystalline Bi_2S_3 . The intensity distribution of the reflection corresponding to the (020) plane, in particular, is narrow, with most of its intensity centered about the meridian. This result is expected since the (020) plane is oriented directly out-of-plane when the nanowires are lying perfectly flat on the substrate. The intensity distributions for the reflections corresponding to the (130), (220), and (120) planes are broader and span a larger range of azimuthal angles. Given that the planes associated with these reflections are also generally normal to the (001) plane that is parallel to the nanowire long axis, the observation that their intensities are generally distributed about the meridian confirms that the nanowires are generally lying in the plane of the substrate. It follows that these out-of-plane reflections that are visible in the GIXD image in Figure 5A correspond to the distribution of planes that are generally parallel to the substrate given the orientation variation of nanowires within the network. **Figure 5B** displays the 2D GIXD image of a Bi_2S_3 :P3HT active layer prior to top electrode deposition. Here, we observe reflections associated with both the crystallographic planes of P3HT and Bi_2S_3 . We have labelled the reflections corresponding to the (100) and (200) planes of P3HT at scattering vectors of $q = 0.37 \text{ \AA}^{-1}$ and 0.74 \AA^{-1} , respectively, for clarity. The intensity anisotropy along the azimuthal angle of these reflections indicate that P3HT is preferentially oriented with the ($h00$) planes parallel to the substrate. Correspondingly, we calculated the Herman's orientation function,^{16, 17} f , of the (100) reflection to quantify the orientation distribution of P3HT within the active layer. As discussed elsewhere,^{16, 17, 73} f_{hkl} can range from 1 to -0.5 wherein $f_{hkl} = 1$ indicates perfect out-of-plane alignment of that (hkl) plane with respect to the substrate; $f_{hkl} = -0.5$ indicates perfect alignment of that (hkl) plane in the plane of the substrate; and $f_{hkl} = 0$ indicates no preferential alignment of that (hkl) plane. We obtained an f_{100} of 0.32. For comparison, f_{100} of 0.45 and 0.42 have been reported for

P3HT in bulk-heterojunction active layers comprising PCBM and ZnO as acceptors, respectively.^{16, 74} This analysis suggests that the P3HT in our active layers is less oriented than those in materials stacks where PCBM or ZnO serve as electron acceptors. We believe the fabrication and incorporation of vertically-oriented Bi₂S₃ scaffolds, as opposed to horizontally-oriented nanowires in networks, could induce further orientation in the P3HT layer.

Conclusions

In summary, we report the assembly of percolated Bi₂S₃ networks via a vacuum-filtration technique and the photovoltaic characterization of such networks as electron acceptors in hybrid solar cells. Efficiencies up to 3.3% was achieved for these devices. While we cannot clearly determine the complete infiltration of P3HT into the voids of our Bi₂S₃ nanowire network, we are confident that there is substantial intermixing between P3HT and Bi₂S₃ nanowire networks. We foresee surface modification of metal chalcogenides via adsorption of self-assembled monolayers as a means to tune the chemical/physical properties of the inorganic-organic interface; this approach was demonstrated to be successful in improving the interfacial compatibility between ZnO nanowires and P3HT, resulting in markedly improved photovoltaic devices.¹⁷

Acknowledgments

This work was supported by ONR's Photovoltaic Program (N00014-11-10328) and NSF through grant CHE-1124754 and CHE-092104 and the Princeton Center for Complex Materials MRSEC (Grant DMR-0819860), which also provided access to the PRISM Imaging and Analysis Center. Partial funding from NRI (Grant Number 2011-NE-2205GB) is also acknowledged. GIXD experiments were conducted at CHESS, which is supported by NSF and NIH/NIGMS under award DMR-0936384. L.W.-B. is supported by the L'Oreal USA for Women in Science post-doctoral fellowship. A.K.H. is supported by an NSF graduate research fellowship. We also acknowledge Prof. Steven L. Bernasek from the Department of Chemistry at Princeton University for allowing us access to his XPS and UPS instrumentation.

Notes and references

^a Department of Chemical and Biological Engineering, Princeton University, Princeton, NJ 08544 email: lloo@princeton.edu

^b Department of Chemistry, Princeton University, Princeton, NJ 08544

^c Princeton Institute for the Science and Technology of Materials, Princeton University, Princeton, NJ 08544

† Electronic Supplementary Information (ESI) available. See DOI: 10.1039/b000000x/

1. K. D. G. I. Jayawardena, L. J. Rozanski, C. A. Mills, M. J. Beliatas, N. A. Nismy and S. R. P. Silva, *Nanoscale*, 2013, **5**, 8411-8427.
2. J. Hou, H.-Y. Chen, S. Zhang, R. I. Chen, Y. Yang, Y. Wu and G. Li, *J. Am. Chem. Soc.*, 2009, **131**, 15586-15587.
3. D. Mühlbacher, M. Scharber, M. Morana, Z. Zhu, D. Waller, R. Gaudiana and C. Brabec, *Adv. Mater.*, 2006, **18**, 2884-2889.
4. N. Blouin, A. Michaud and M. Leclerc, *Adv. Mater.*, 2007, **19**, 2295-2300.
5. S. H. Park, A. Roy, S. Beaupré, S. Cho, N. Coates, J. S. Moon, D. Moses, M. Leclerc, K. Lee and A. J. Heeger, *Nat. Photonics*, 2009, **3**, 297-302.
6. A. M. Smith and S. Nie, *Accounts Chem. Res.*, 2009, **43**, 190-200.
7. B. Sun and N. C. Greenham, *Phys. Chem. Chem. Phys.*, 2006, **8**, 3557-3560.
8. B. Sun, H. J. Snaith, A. S. Dhoot, S. Westenhoff and N. C. Greenham, *J. Appl. Phys.*, 2005, **97**, 014911/1-014914/6.
9. S. Dayal, N. Kopidakis, D. C. Olson, D. S. Ginley and G. Rumbles, *Nano Lett.*, 2009, **10**, 239-242.
10. N. C. Greenham, X. Peng and A. P. Alivisatos, *Phys. Rev. B*, 1996, **54**, 17628-17637.
11. Y.-Y. Lin, T.-H. Chu, S.-S. Li, C.-H. Chuang, C.-H. Chang, W.-F. Su, C.-P. Chang, M.-W. Chu and C.-W. Chen, *J. Am. Chem. Soc.*, 2009, **131**, 3644-3649.
12. J. Liu, E. N. Kadnikova, Y. Liu, M. D. McGehee and J. M. J. Fréchet, *J. Am. Chem. Soc.*, 2004, **126**, 9486-9487.
13. K. M. Coakley and M. D. McGehee, *Appl. Phys. Lett.*, 2003, **83**, 3380-3382.
14. H.-S. Shim, J. W. Kim, Y.-E. Sung and W. B. Kim, *Sol. Energ. Mat. Sol. C.*, 2009, **93**, 2062-2068.
15. Y. S. Kim, B.-K. Yu, D.-Y. Kim and W. B. Kim, *Sol. Energ. Mat. Sol. C.*, 2011, **95**, 2874-2879.
16. L. Whittaker-Brooks, J. M. Mativetsky, A. Woll, D. Smilgies and Y.-L. Loo, *Org. Electron.*, 2013, **14**, 3477-3483.
17. L. Whittaker-Brooks, W. E. McClain, J. Schwartz and Y.-L. Loo, *Adv. Energy Mater.*, 2014, **4**, 1400585/1-1400585/7.
18. Y.-J. Lee, M. T. Lloyd, D. C. Olson, R. K. Grubbs, P. Lu, R. J. Davis, J. A. Voigt and J. W. P. Hsu, *J. Mater. Chem. C*, 2009, **113**, 15778-15782.
19. D. C. Olson, Y.-J. Lee, M. S. White, N. Kopidakis, S. E. Shaheen, D. S. Ginley, J. A. Voigt and J. W. P. Hsu, *J. Mater. Chem. C*, 2007, **111**, 16640-16645.
20. D. C. Olson, J. Piris, R. T. Collins, S. E. Shaheen and D. S. Ginley, *Thin Solid Films*, 2006, **496**, 26-29.
21. L. Baeten, B. Conings, H.-G. Boyen, J. D'Haen, A. Hardy, M. D'Olieslaeger, J. V. Manca and M. K. Van Bael, *Adv. Mater.*, 2011, **23**, 2802-2805.
22. L. Baeten, B. Conings, J. D'Haen, C. De Dobbelaere, A. Hardy, J. V. Manca and M. K. Van Bael, *ChemPhysChem*, 2012, **13**, 2777-2783.
23. D. Chi, S. Qu, Z. Wang and J. Wang, *J. Mater. Chem. C*, 2014, **2**, 4383-4387.
24. G. Li, V. Shrotriya, J. Huang, Y. Yao, T. Moriarty, K. Emery and Y. Yang, *Nat. Mater.*, 2005, **4**, 864-868.
25. A. a. F. Eftaiha, J.-P. Sun, I. G. Hill and G. C. Welch, *J. Mater. Chem. A*, 2014, **2**, 1201-1213.
26. S. A. McDonald, G. Konstantatos, S. Zhang, P. W. Cyr, E. J. D. Klem, L. Levina and E. H. Sargent, *Nat. Mater.*, 2005, **4**, 138-142.
27. J. Seo, M. J. Cho, D. Lee, A. N. Cartwright and P. N. Prasad, *Adv. Mater.*, 2011, **23**, 3984-3988.
28. D. Cui, J. Xu, T. Zhu, G. Paradee, S. Ashok and M. Gerhold, *Appl. Phys. Lett.*, 2006, **88**, 18311/1-18311/4.
29. T. Rath, M. Edler, W. Haas, A. Fischeherder, S. Moscher, A. Schenk, R. Trattnig, M. Sezen, G. Mauthner, A. Pein, D. Meischler, K. Bartl, R. Saf, N. Bansal, S. A. Haque, F. Hofer, E.

- J. W. List and G. Trimmel, *Adv. Energy Mater.*, 2011, **1**, 1046-1050.
30. L.-I. Hung, C.-K. Tsung, W. Huang and P. Yang, *Adv. Mater.*, 2010, **22**, 1910-1914.
31. L. Martinez, M. Bernechea, F. P. G. de Arquer and G. Konstantatos, *Adv. Energy Mater.*, 2011, **1**, 1029-1035.
32. A. K. Rath, M. Bernechea, L. Martinez and G. Konstantatos, *Adv. Mater.*, 2011, **23**, 3712-3717.
33. H.-C. Liao, M.-C. Wu, M.-H. Jao, C.-M. Chuang, Y.-F. Chen and W.-F. Su, *CrystEngComm*, 2012, **14**, 3645-3652.
34. L. Martinez, A. Stavrinadis, S. Higuchi, S. L. Diedenhofen, M. Bernechea, K. Tajima and G. Konstantatos, *Phys. Chem. Chem. Phys.*, 2013, **15**, 5482-5487.
35. A. J. MacLachlan, F. T. F. O'Mahony, A. L. Sudlow, M. S. Hill, K. C. Molloy, J. Nelson and S. A. Haque, *ChemPhysChem*, 2014, **15**, 1019-1023.
36. L. Yun-Yue, W. Di-Yan, Y. Hung-Chi, C. Hsuen-Li, C. Chia-Chun, C. Chun-Ming, T. Chih-Yuan and C. Chun-Wei, *Nanotechnology*, 2009, **20**, 405207.
37. D. S. Ginger and N. C. Greenham, *Phys. Rev. B*, 1999, **59**, 10622-10629.
38. S. Ren, N. Zhao, S. C. Crawford, M. Tambe, V. Bulović and S. Gradečak, *Nano Lett.*, 2010, **11**, 408-413.
39. H. Moreno-García, M. T. S. Nair and P. K. Nair, *Thin Solid Films*, 2011, **519**, 7364-7368.
40. K. Biswas, L.-D. Zhao and M. G. Kanatzidis, *Adv. Energy Mater.*, 2012, **2**, 634-638.
41. Z.-H. Ge, B.-P. Zhang, P.-P. Shang and J.-F. Li, *J. Mater. Chem.*, 2011, **21**, 9194-9200.
42. Q. Yang, C. Hu, S. Wang, Y. Xi and K. Zhang, *J. Phys. Chem. C*, 2013, **117**, 5515-5520.
43. G.-Y. Liu, L.-Y. Xu, F. Zhou, Y. Zhang, H. Li, Q. F. Xu and J. M. Lu, *Phys. Chem. Chem. Phys.*, 2013, **15**, 11554-11558.
44. E. Pineda, M. E. Nicho, P. K. Nair and H. Hu, *Sol. Energy*, 2012, **86**, 1017-1022.
45. G. Konstantatos, L. Levina, J. Tang and E. H. Sargent, *Nano Lett.*, 2008, **8**, 4002-4006.
46. L. Martinez, S. Higuchi, A. J. MacLachlan, A. Stavrinadis, N. C. Miller, S. L. Diedenhofen, M. Bernechea, S. Sweetnam, J. Nelson, S. A. Haque, K. Tajima and G. Konstantatos, *Nanoscale*, 2014, **6**, 10018-10026.
47. J. Ma, J. Yang, L. Jiao, T. Wang, J. Lian, X. Duan and W. Zheng, *Dalton T.*, 2011, **40**, 10100-10108.
48. R. Chen, M. H. So, C.-M. Che and H. Sun, *J. Mater. Chem.*, 2005, **15**, 4540-4545.
49. W. Lou, M. Chen, X. Wang and W. Liu, *Chem. Mater.*, 2007, **19**, 872-878.
50. Q. Han, J. Chen, X. Yang, L. Lu and X. Wang, *J. Phys. Chem. C*, 2007, **111**, 14072-14077.
51. Y. W. Koh, C. S. Lai, A. Y. Du, E. R. T. Tiekink and K. P. Loh, *Chem. Mater.*, 2003, **15**, 4544-4554.
52. Z. Wu, Z. Chen, X. Du, J. M. Logan, J. Sippel, M. Nikolou, K. Kamaras, J. R. Reynolds, D. B. Tanner, A. F. Hebard and A. G. Rinzler, *Science*, 2004, **305**, 1273-1276.
53. J. Bok Kim, S. Ahn, S. Ju Kang, C. Nuckolls and Y.-L. Loo, *Appl. Phys. Lett.*, 2013, **102**, 103302/1-103302-4.
54. D.-M. Smilgies, D. R. Blasini, S. Hotta and H. Yanagi, *J. Synchrotron Rad.*, 2005, **12**, 807-811.
55. D.-M. Smilgies, *J. Appl. Cryst.*, 2009, **42**, 1030-1034.
56. D.-M. Smilgies and D. R. Blasini, *J. Appl. Cryst.*, 2007, **40**, 716-718.
57. B. C. Thompson and J. M. J. Fréchet, *Angew. Chem. Int. Edit.*, 2008, **47**, 58-77.
58. M. D. Irwin, D. B. Buchholz, A. W. Hains, R. P. H. Chang and T. J. Marks, *P. Natl. A. Sci.*, 2008, **105**, 2783-2787.
59. P. P. Khlyabich, B. Burkhart, A. E. Rudenko and B. C. Thompson, *Polymer*, 2013, **54**, 5267-5298.
60. Z.-L. Guan, J. Bok Kim, Y.-L. Loo and A. Kahn, *J. Appl. Phys.*, 2011, **110**, 043719/1-043719/5.
61. Z.-L. Guan, J. B. Kim, H. Wang, C. Jaye, D. A. Fischer, Y.-L. Loo and A. Kahn, *Org. Electron.*, 2010, **11**, 1779-1785.
62. J. Grigas, E. Talik and V. Lazauskas, *Phys. Status Solidi (b)*, 2002, **232**, 220-230.
63. F. T. Chuang, P. Y. Chen, T. C. Cheng, C. H. Chien and B. J. Li, *Nanotechnology*, 2007, **18**, 395702.
64. C. D. Wagner, L. E. Davis, M. V. Zeller, J. A. Taylor, R. H. Raymond and L. H. Gale, *Surf. Interface Anal.*, 1981, **3**, 211-225.
65. M. C. Scharber, D. Mühlbacher, M. Koppe, P. Denk, C. Waldauf, A. J. Heeger and C. J. Brabec, *Adv. Mater.*, 2006, **18**, 789-794.
66. H. J. Snaith, *Energ. Environ. Sci.*, 2012, **5**, 6513-6520.
67. P. Docampo, J. M. Ball, M. Darwich, G. E. Eperon and H. J. Snaith, *Nat. Commun.*, 2013, **4**, 1-6.
68. M. M. Lee, J. Teuscher, T. Miyasaka, T. N. Murakami and H. J. Snaith, *Science*, 2012, **338**, 643-647.
69. D.-Y. Son, J.-H. Im, H.-S. Kim and N.-G. Park, *J. Phys. Chem. C*, 2014, **118**, 16567-16573.
70. Y. C. Choi, Y. H. Lee, S. H. Im, J. H. Noh, T. N. Mandal, W. S. Yang and S. I. Seok, *Adv. Energy Mater.*, 2014, **4**, 1301680/1-1301680/5.
71. H. Zhou, Q. Chen, G. Li, S. Luo, T.-b. Song, H.-S. Duan, Z. Hong, J. You, Y. Liu and Y. Yang, *Science*, 2014, **345**, 542-546.
72. H. Mizoguchi, H. Hosono, N. Ueda and H. Kawazoe, *J. Appl. Phys.*, 1995, **78**, 1376-1378.
73. A. M. Hiszpanski, S. S. Lee, H. Wang, A. R. Woll, C. Nuckolls and Y.-L. Loo, *ACS Nano*, 2012, **7**, 294-300.
74. J. K. Keum, K. Xiao, I. N. Ivanov, K. Hong, J. F. Browning, G. S. Smith, M. Shao, K. C. Littrell, A. J. Rondinone, E. Andrew Payzant, J. Chen and D. K. Hensley, *CrystEngComm*, 2013, **15**, 1114-1124.

